



HAL
open science

Thermal behaviour of caesium implanted in UO₂: A comparative study with the xenon behaviour

C. Panetier, Y. Pipon, C. Gaillard, N. Moncoffre, T. Wiss, D. Mangin, O. Dieste, B. Marchand, R. Ducher, R. Dubourg, et al.

► **To cite this version:**

C. Panetier, Y. Pipon, C. Gaillard, N. Moncoffre, T. Wiss, et al.. Thermal behaviour of caesium implanted in UO₂: A comparative study with the xenon behaviour. *Journal of Nuclear Materials*, 2021, 543, pp.152520. 10.1016/j.jnucmat.2020.152520 . hal-02955726

HAL Id: hal-02955726

<https://hal.science/hal-02955726>

Submitted on 27 Nov 2020

HAL is a multi-disciplinary open access archive for the deposit and dissemination of scientific research documents, whether they are published or not. The documents may come from teaching and research institutions in France or abroad, or from public or private research centers.

L'archive ouverte pluridisciplinaire **HAL**, est destinée au dépôt et à la diffusion de documents scientifiques de niveau recherche, publiés ou non, émanant des établissements d'enseignement et de recherche français ou étrangers, des laboratoires publics ou privés.

Thermal behaviour of caesium implanted in UO₂: a comparative study with the xenon behaviour

C. Panetier^a, Y. Pison^{a,b,*}, C. Gaillard^a, N. Moncoffre^a, T. Wiss^c, D. Mangin^d, O. Dieste^c, B. Marchand^a, R. Ducher^e, R. Dubourg^e, T. Epicier^f, L. Raimbault^g

^a Univ Lyon, Univ Claude Bernard Lyon 1, CNRS/IN2P3, IP2I Lyon, UMR 5822, F-69622, Villeurbanne, France

^b Univ Lyon, UCBL, IUT Lyon-1, Département chimie, F-69622, Lyon, France

^c European Commission, DG Joint Research Centre, Directorate G – Nuclear Safety & Security, PO box 2340, D-76125 Karlsruhe, Germany

^d ILL, Université de Lorraine, CNRS : UMR7198 – CS 14234 54042 Nancy Cedex, France

^e IRSN, LETR – BP3 13115 St-Paul-Lez-Durance Cedex, France

^f Univ Lyon, INSA Lyon, Univ Claude Bernard Lyon 1, CLYM, MATEIS, UMR CNRS 5510, 7, avenue Jean-Capelle, 69621 Villeurbanne cedex, France

^g MINES ParisTech, PSL Research University, Centre de Géosciences, 35 rue St Honoré 77305 Fontainebleau, France

Keywords: UO₂, SIMS, TEM, Cs, Xe, bubbles

*** Corresponding author:** Yves PIPON

E-mail: y.pipon@ipnl.in2p3.fr

Postal address: Université de Lyon, UCBL, IP2I, Campus LyonTech La Doua, 4 rue Enrico Fermi, 69622 Villeurbanne cedex, France

Highlights

- SIMS and TEM techniques were combined to compare the thermal behaviour of Cs and Xe in UO₂.
- Both elements form bubbles with different growth kinetics.
- At 1600 °C, caesium is found to be highly mobile in the UO₂ matrix while Xe distribution does not evolve.

Abstract

Xenon and caesium are among the most impacting fission products when studying the nuclear fuel: xenon for its role on the fuel rod thermomechanical behaviour during reactor operation and caesium in the case of atmospheric radioactive release during an accident in a nuclear power plant. This paper focuses on the comparison of caesium and xenon thermal behaviour in polycrystalline uranium dioxide (UO_2) pellets. Caesium-133 or xenon-136 stable isotopes were introduced in depleted UO_2 samples by ion implantation at a maximum concentration of 0.08 at. % at a depth of around 140 nm below the sample surface. Annealing under reducing atmosphere (Ar/H_2 5 %) was performed at 1000 °C or 1600 °C, which corresponds respectively to a representative temperature during nuclear reactor operation (at the center of the fuel pellets) and during an accident. The caesium migration in UO_2 was investigated by Secondary Ion Mass Spectrometry and compared to the thermal behaviour of xenon in UO_2 at 1600 °C. Transmission Electron Microscopy was performed in order to characterise UO_2 microstructure before and after annealing. The results indicate that caesium has a different behaviour than xenon with which it is often compared for its release from the nuclear fuel. In particular, we highlight a difference between the growth kinetics of caesium and of xenon bubbles at 1600 °C which can be correlated to the availability of thermal vacancies in UO_2 and to the different ability of Xe and Cs atoms for thermal resolution.

1. Introduction

Nuclear accidents can cause a tremendous release of various radionuclides into the environment. The main volatile radionuclides of concern in such events are the rare gases (mainly xenon) but also the volatile fission products (FP), in particular iodine and caesium. One of the radionuclides with the longest half-life detected in the environment after the accident of Fukushima Daichii (2011) is caesium-137 (30.1 years of half-life) with a contamination exceeding 600 000 Bq m⁻² on 600 km² around the Fukushima power plants [1]. Caesium release and dispersion is therefore of major impact in the case of a nuclear accident due also to its biological similarity with potassium. In the UO₂ nuclear fuel used in light water reactors (LWR), it is also one of the most abundant FP. Indeed, seven atoms of caesium-135 and six atoms of caesium-137 are produced per 100 ²³⁵U fissions. For a uranium oxide fuel (UOx) with a burnup of 45 GW·d·t_U⁻¹, it represents an accumulation of 4 kg of caesium per 1 ton of uranium, which means a concentration of around 0.7 at. % [2]. Predicting the release of FP during a nuclear reactor accident can be supported by laboratory tests on irradiated fuels including in oxidative conditions [3]. To that extent, several studies were dedicated to measure the FP global release from irradiated nuclear fuel in accidental conditions, such as PHEBUS, VERCORS or VEGA integral research programs [4-6]. For instance, during VERCORS tests (in reducing conditions), it was observed that the caesium release starts at relatively low temperature, *i.e.* 1200 °C and is complete at 2300 °C, which supports that caesium is categorized as a volatile element. Several studies have investigated the Cs release as a function of irradiation and temperature conditions. Peehs *et al.*, in [7], have measured the Cs release from LWR irradiated fuel at different burnup in a resistance-heated Knudsen cell under vacuum. They have observed that, for a burnup of 10.9 GW·d·t_U⁻¹, the release started at 1800 °C while at higher burnup, 33 GW·d·t_{HM}⁻¹, it started at 1400 °C. Inductively coupled plasma mass spectrometry measurements performed by Scherbina *et al.* have shown that Cs release from irradiated fuel occurred at 1450 °C and was complete at 2000 °C under reducing atmosphere [8]. In their study of fission gas and volatile fission products from a very high local burnup LWR UO₂ fuel *i.e.* 240 GW·d·t_{HM}⁻¹, Hiernaut *et al.* [9] have shown that both fission gases and caesium show a similar trend in the release from the high burnup structure using a Knudsen cell under vacuum. There is a first release around 1000 K (725 °C) followed by a substantial release of these elements at around 1400 K (1125 °C). Whereas the onset for release of the fission gases and caesium is the same in both stages, the shape of the release of the second stage is smoother for the case of the caesium. Further studies have been performed on oxidized irradiated fuel by Hiernaut *et al.* [10]. In a 65 GW·d·t_{HM}⁻¹ pre-oxidised fuel sample, it was observed that caesium starts to be steadily released from 600 K (325 °C) until 1250 K (975 °C) coinciding with the start of the sample reduction from U₃O₈ to U₄O₉. The complete release was obtained for a temperature of 1850 K (1575 °C). In post irradiation experiments, Prussin *et al.* have

measured a Cs release of 31 % of the inventory from irradiated depleted UO₂ pellets annealed at 1750 °C under a flow of H₂ gas containing a small impurity of H₂O (~70 ppm) [11]. From these studies, and the release kinetics trends, the Cs release appears to be very sensitive to temperature, burnup and irradiation history of the fuel. According to Walker *et al.*, Cs being gaseous from 1200 °C, its behaviour should be similar to Xe above this temperature [12]. This is in accordance with data obtained during the VERDON high temperature annealing experiments [13], which have highlighted quite close release kinetics between Xe, Kr and Cs. However, below 1200 °C, in some external radial part of the pellets, Desgranges *et al.* have pointed out that caesium was trapped whereas xenon was fully released after a power transient in an irradiated fuel [14-15]. In these papers, the authors have concluded that the caesium transport is driven by the strong temperature gradient between the centre (up to 1800 °C during power transient) and the periphery of the pellet (down to 400 °C). The immobilization of the caesium is associated by these authors with the formation of caesium uranates solid phases but this hypothesis was not proven. Being often compared to xenon, very few data are available on caesium migration under the sole effect of temperature. The few Cs diffusion coefficients available in the literature were determined with the Booth model [16] from the Cs release measurements after irradiation of UO₂ pellets [5, 9].

Therefore, in spite of numerous studies about FP release in normal and accidental conditions, uncertainties remain about the state and behaviour of caesium in the nuclear fuel. The present study aims at giving insights into the mechanisms lying behind the Cs thermal behaviour in UO₂ at 1600 °C by comparing results between data obtained on caesium and on xenon.

To address these objectives, Cs and Xe implanted UO₂ pellets were annealed at temperatures representative of normal and accidental conditions in a LWR fuel. Secondary Ion Mass Spectrometry (SIMS) was used to measure depth profiles before and after annealing. The aim is to characterise migration mechanisms depending on the profile evolution induced by the different annealing conditions. The SIMS technique has already been successfully used to study the behaviour of elements easily ionised in UO₂, such as iodine [17-18], chlorine [19] but also molybdenum in UO₂ and UO_{2+x} [20]. The inert gases (He, Kr and Xe) are difficult to ionise and their measurements are therefore challenging by SIMS. However, the feasibility of quantitative analyses has been already demonstrated for Kr in uranium-based materials [21-22] and for Xe in UO₂ [23].

The present investigation relies on the coupling of SIMS depth profiling with TEM (Transmission Electron Microscopy) characterisations. Indeed, TEM allows characterising the quantity and nature of some defects created by Cs or Xe implantation before and after annealing. Extended defects and other features such as bubbles are quantified with respect to the implantation depth and correlated to the depth profiles obtained by SIMS.

2. Material and methods

In this study, depleted UO_2 pellets (0.2 at. % of ^{235}U) supplied by FRAMATOME (ex-AREVA NP) were sintered at $1750\text{ }^\circ\text{C}$ under a reducing atmosphere ($\text{Ar}/\text{H}_2\text{-5\%}$) during 5 h in order to set up a stoichiometry of $\text{UO}_{2.00}$ and a high bulk density value (97.5 % of the theoretical density). Each pellet is a disk with a height of (1.7 ± 0.2) mm and diameter of (8.6 ± 0.4) mm. The mean grain size distribution is centred at around $11\text{ }\mu\text{m}$, which is the standard average grain size in LWR fuel.

The pellets were polished on one side by the PRIMEVerre company (Montpellier, France). In order to analyse the surface texture after polishing, optic interferometry measurements on a FOGALE NANOTECH device were performed at the LaMCoS laboratory, INSA Lyon, France. The mean roughness was found to be 5 nm. The samples were subsequently annealed at $1000\text{ }^\circ\text{C}$ during 10 h in a PECKLY© tubular furnace under vacuum (10^{-7} mbar) in order to degas particles adsorbed on the surface. Then, the samples were annealed at $1600\text{ }^\circ\text{C}$ for 4 h in a NABERTHERM© tubular furnace under a 5 % H_2/Ar gas mixture in order to anneal the polishing damage while maintaining the $\text{UO}_{2.00}$ stoichiometry. This procedure removes damage at the sample surface, which was verified by performing Doppler Broadening Positron Annihilation Spectroscopy measurements [24].

Caesium or xenon ions were introduced in the pellets by ion implantation. This well-known technique has been extensively used to study diffusion of fission products in oxide nuclear fuels. Afterwards, some of the as-implanted samples were annealed either at $1000\text{ }^\circ\text{C}$ or at $1600\text{ }^\circ\text{C}$ in the NABERTHERM© furnace under reducing atmosphere (5 % H_2/Ar). The caesium or xenon distributions were measured before and after annealing by SIMS and the microstructural changes were observed by TEM.

Table 1 gathers all the characterisations made on the implanted (with caesium or xenon) samples used in this work.

Table 1- list of characterisations by SIMS or TEM made on samples implanted with Cs or Xe ($10^{15}\text{ at}\cdot\text{cm}^{-2}$) and subsequently annealed at $1000\text{ }^\circ\text{C}$ or $1600\text{ }^\circ\text{C}$.

Annealing conditions	Analysed by SIMS	Analysed by TEM
No annealing	Cs or Xe	Cs
$1000\text{ }^\circ\text{C}$ (4h)	Cs	Cs
$1600\text{ }^\circ\text{C}$ (3h or 4h)	Cs or Xe	-
$1600\text{ }^\circ\text{C}$ (12h)	Cs or Xe	Cs or Xe
$1600\text{ }^\circ\text{C}$ (16h)	Xe	-

3. Experimental details

3.1 Caesium and xenon implantation

The samples were implanted with 800 keV $^{133}\text{Cs}^{2+}$ ions or 800 keV $^{136}\text{Xe}^{2+}$ ions at IP2I (Institut de Physique des deux Infinis) Lyon, France using the IMIO400 accelerator facility with a cooling device maintaining the sample temperature at 15 °C and under vacuum ($< 5 \times 10^{-6}$ mbar) preventing any oxidation. An implantation fluence of 10^{15} at·cm⁻² was chosen as a compromise between the low sensitivity of the xenon detection by SIMS and the need to avoid, as far as possible, the creation of too many defects which could mask small clusters or small precipitates in the material. This fluence is estimated to be representative of the Cs and Xe concentration in a nuclear fuel with a low burnup value (around 4 GW·d·t_U⁻¹).

Simulation of the Cs or Xe implantation profiles and energy losses was performed using the SRIM 2013 software [25] in the full cascade mode. We considered a density of 10.7 g·cm⁻³ and displacement energies were set to 40 eV and 20 eV for uranium atoms and oxygen atoms respectively as determined by Soullard *et al.* [26]. The resulting Cs and Xe depth profiles are quasi identical. They are Gaussian distributions with a maximum concentration of 0.08 at.% at a projected range of 140 nm with a straggling of 65 nm. The damage distribution peak is located at around 80 nm for a maximum value of 8 dpa (displacements per atom).

3.2 SIMS analyses

In UO₂ poly-crystalline samples, the sputter velocity and the secondary ion yield are known to strongly depend on the crystalline orientation of each single grain [27], which can in turn strongly affect the SIMS depth profile measure of the studied element. For a typical SIMS raster size (200 μm x 200 μm), a large number of grains (typically 100) is analysed when the sample is constituted of small grains (around 5 μm), so the effects due to the different grain orientations are averaged out. This was highlighted by Marchand *et al.* [23] who performed SIMS analysis on UO₂ samples with two different grain sizes (7 μm and 22 μm). A methodology similar to the Relative Sensitive Factor (RSF) introduced by Wilson [28] was successfully used to determine the depth profiles of xenon in small UO₂ grains but some discrepancies were observed for samples with large grains. In the present study, the UO₂ grain size is larger than 10 μm so that the SIMS analysis area covers only a few grains. We have thus carried out two different methodologies described below to offset the effect of the preferential grain sputtering on the SIMS spectra.

First, SIMS analyses of Xe implanted samples were performed on a CAMECA IMS 6f instrument at the *Ecole des Mines of Paris* (France). A primary beam of 15 keV O_2^+ ions with a current of 90 nA was used. The raster surface size was $150 \times 150 \mu m^2$. Secondary ions ($^{238}U^{16}O^+$ and $^{136}Xe^+$) were collected in the raster central part (62 μm diameter) to avoid side-wall effects. They were first accelerated by a +4.5 kV electrical potential and then analysed by a mass spectrometer. Difficulties in measuring the xenon signal arise from its high ionization energy, which explains the low sensitivity of this gas by SIMS. The ionization of xenon is done above the surface when the sputtered atoms interact with the O^{2+} ions primary beam [27]. After the analyses, a homemade software called Sims Depth Profile Achievement [29] was used to process the collected raw data taking into account the different sputtering velocities of the different grains. At least three measurements were performed on each sample in order to verify the depth profile reproducibility.

Secondly, SIMS analyses of Cs implanted samples were performed on a CAMECA IMS 7f facility at the Jean Lamour Institute (IJL), Nancy, France. This instrument is equipped with a eucentric rotating sample stage (see [30] for details) designed by CAMECA to improve the depth resolution by inhibiting the surface roughening during SIMS analyses of poly-crystalline materials. We have shown in a previous work that the use of the eucentric rotating stage with a 15 rpm velocity for UO_2 samples implanted with molybdenum significantly improves the reproducibility of the measurements [30]. In the present study, a primary beam of 10 keV O_2^+ ions with a current of 140 nA was used. The raster size was $250 \times 250 \mu m^2$ on the UO_2 sample surfaces and the velocity of the eucentric stage was set to 8 rpm after some calibrations. Secondary ions ($^{238}U^{16}O^+$ and $^{133}Cs^+$) were collected on the raster central part (62 μm diameter). The conversion of chronograms into depth profiles is detailed hereafter. First, the sputtering time was converted into depth by calculating the sputtering velocity. This was done by dividing the raster depth value, measured by optical interferometry at the LaMCoS laboratory, by the final acquisition time. The depth resolution obtained is about 10 nm. The intensity of the Cs signal was converted into atomic concentration thanks to the RSF, which is expressed in equation (eq. 1).

$$RSF = \frac{\varphi \times \overline{I_{UO}}}{\left(\sum_{i=0}^{final\ time} I_i - (I_{bgd} \times n_{cycle})\right) \times t_{cycle} \times v_{sputter}} \quad (\text{eq. 1})$$

With: φ , the implantation fluence ($10^{15} \text{ Cs}\cdot\text{cm}^{-2}$)

$\overline{I_{UO}}$, the averaged $^{254}UO^+$ signal taken as an internal reference (in $\text{counts}\cdot\text{s}^{-1}$)

I_i , the intensity of the collected specie « i » at a specific time (in $\text{counts}\cdot\text{s}^{-1}$)

$I_{bgd} \times n_{cycle}$, the intensity of the background signal for the number « n » of measured cycles (in $\text{counts}\cdot\text{s}^{-1}$)

t_{cycle} , the duration of each cycle (in seconds)

$v_{sputter}$, the sputtering velocity (in $\text{cm}\cdot\text{s}^{-1}$)

A statistic error was determined by performing 11 analyses on two different Cs as-implanted samples. We determined a RSF value of $(1.6 \pm 0.3) \times 10^{20} \text{ at}\cdot\text{cm}^{-3}$. This value is of the same order of magnitude than the one found for Cs in silicon [28]. This is a low value, which indicates the ease of ionizing caesium implanted in UO_2 and we can therefore estimate a limit of detection around 100 ppb.

For each SIMS analysis of a given sample, at least three craters were made and consequently three depth profiles were obtained which were further averaged. Figure 1 presents three depth profiles of caesium (Figure 1.a) or xenon (Figure 1.b) implanted in UO_2 samples and analysed with the methodology described before for each element. These profiles are compared with the depth profiles calculated with the SRIM software. There is a good reproducibility between the curves of the different rasters and a fairly good agreement with the SRIM profile with only a small deviation for the projected range ($\sim 125 \text{ nm}$ for the SIMS analysis).

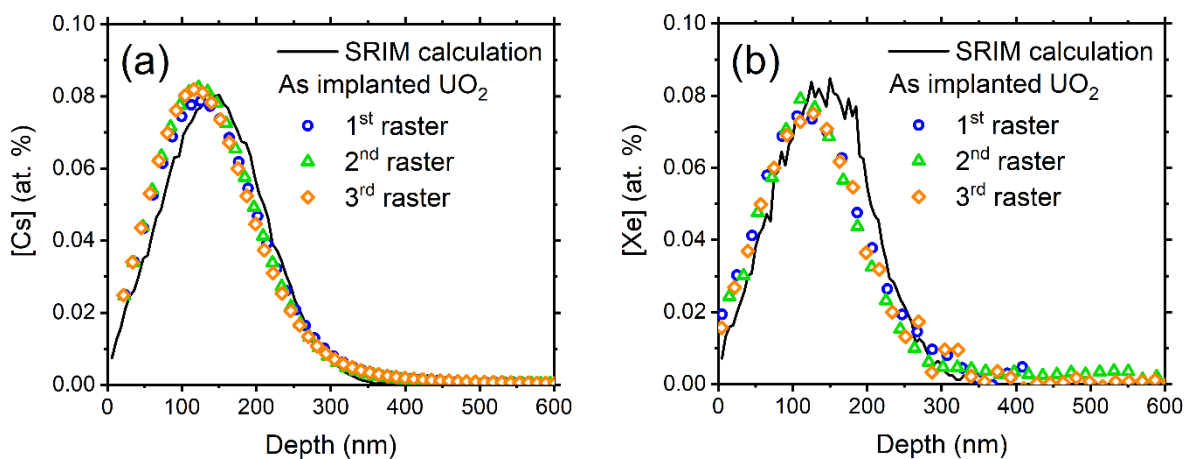


Figure 1- Three depth profiles obtained with SIMS on caesium (a) and xenon (b) as-implanted samples ($10^{15} \text{ at}\cdot\text{cm}^{-2}$) compared to the depth profile calculated with the SRIM software.

3.3 TEM analyses

Focused Ion Beam (FIB) was used to cut lamellae from the UO_2 samples. Their preparation was done by SERMA Technologie at Grenoble, France for samples implanted with xenon and at the JRC (Joint Research Centre) Karlsruhe, Germany for samples implanted with caesium. The implanted samples were first covered with a 100-200 nm gold layer in order to protect the surface from the platinum deposit that in addition protect the area of interest on the sample during FIB operation. Once the Pt deposit was made, two trenches were cut with a Ga^+ ion beam. The part remaining between the two trenches forms the lamella, which was cut from the sample after a pre-thinning and removed with an omniprobe needle. Then, thinning and cleaning of the lamella were performed with the Ga^+ beam (with

care not to destroy the protecting layer). The thickness of each lamella is around 70 nm as determined *via* Electron Energy Loss Spectroscopy by calculating the ratio between the zero loss peak and the total counts considering the total inelastic mean free path and the sample composition.

TEM examinations were performed at the JRC Karlsruhe with a 120 keV electron beam on a Tecnai G2 TEM FEI microscope [31] for the UO₂ samples implanted with caesium and at INSA Lyon (CLYM) on a 200 keV JEOL 2010F microscope for the UO₂ samples implanted with xenon. Both microscopes are equipped with a HAADF detector (High-Angle Annular Dark Field) for STEM images. In the latter imaging mode where a small electron probe is scanned over the region of interest, the detected intensity varies almost proportionally to the density of atoms and to the square of their atomic number. STEM (H)AADF images can therefore provide complementary information on bubbles or voids in comparison with conventional bright field micrographs where diffraction and dynamic effects may limit and/or distort their visibility. After FIB operation, some surface defects remain on the lamellae. These defects, however, are small in size and in concentration and do not interfere with the defects created by ion implantation. Figure 2 displays a TEM image of a virgin UO₂ sample that will be thus the reference image for further comparison with implanted and annealed UO₂ micrographs. In the picture of Figure 2, the residual defects left by the FIB preparation are the dark grey dots which are attributed to defect clusters or to small dislocation loops as reported by He *et al.* in [32] for example. Their size do not exceed 5 nm.

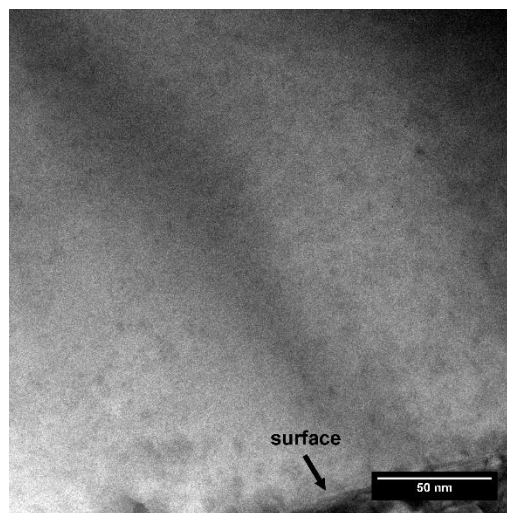


Figure 2- TEM bright field image of a virgin UO₂ sample.

4. Results

4.1 Caesium and xenon depth profiles evolution

Figure 3.a displays the evolution of Cs depth profiles in UO₂ after annealing at 1000 °C and at 1600 °C, and of Xe depth profiles in UO₂ after annealing at 1600 °C (Figure 3.b) under reducing atmosphere.

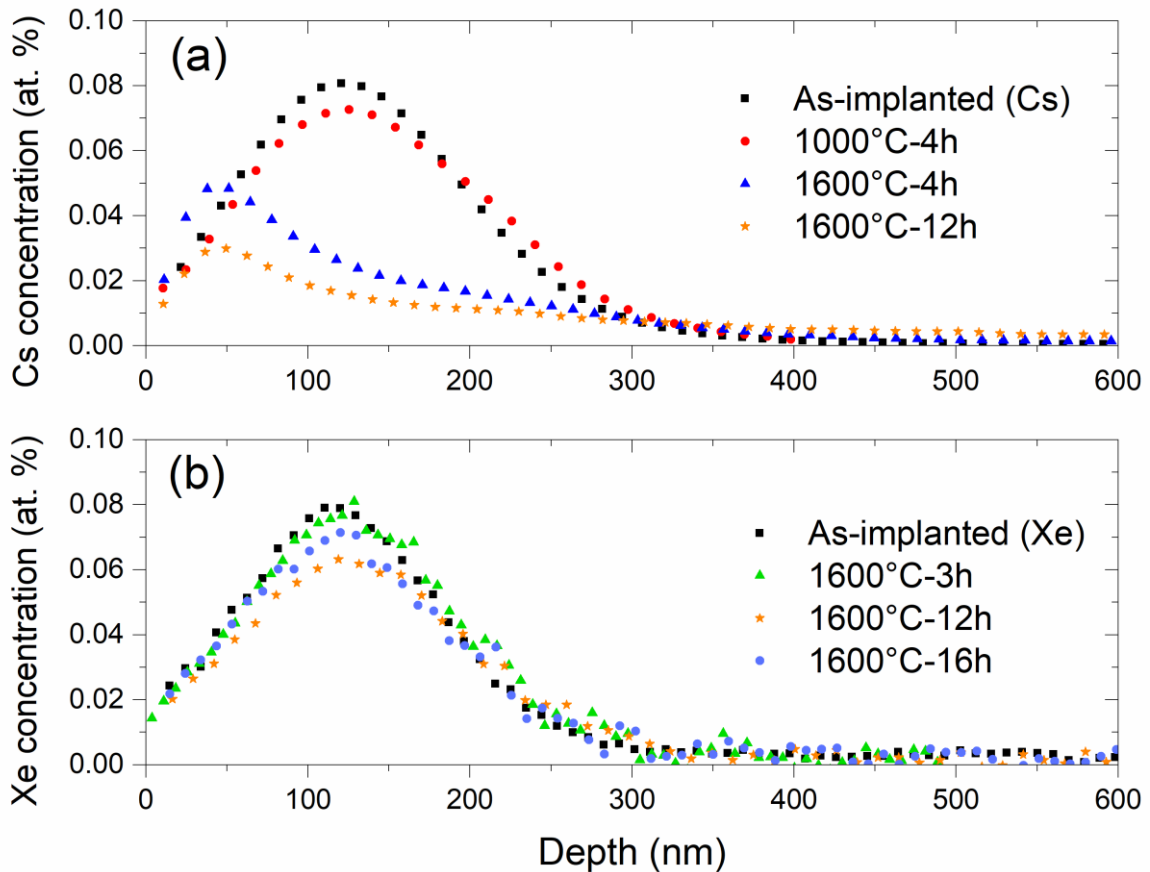


Figure 3- Caesium (a) and xenon (b) depth profiles measured by SIMS in UO_2 samples as a function of annealing temperature (1000 °C or 1600 °C) and compared to the as-implanted depth profile ($10^{15} \text{ at}\cdot\text{cm}^{-2}$).

No significant evolution of the xenon depth profile is observed after annealing at 1600 °C up to 16 hours. This means that no apparent diffusion or release of xenon occurs during these annealing. The caesium depth profile corresponding to the sample annealed at 1000 °C has little evolved compared to the as-implanted one. Only a small decrease of the concentration and a small deviation near 220 nm can be seen. No caesium release has been measured and no significant diffusion is observed. The somewhere low Cs and Xe concentrations can be one part of explanation for the low release also observed in irradiated fuel for equivalent low burn up.

On the contrary, the shape of the Cs depth profiles after annealing at 1600 °C is very different. First, at around 50 nm from the surface, a peak representative of a caesium accumulation is observed. Then, a small shoulder located at around 220 nm is noticed. Finally, a significant diffusion tail is observed in the 1600 °C-12 h sample, which was not visible in the as-implanted profile. It is ascribed to a caesium migration towards the bulk, which is still observed up to a depth of around 1 μm (not shown in Figure 3). The caesium global release can be calculated from the comparison between the depth profile areas

of the as-implanted sample with those of the annealed samples. It was estimated to: (i) 38 % after a 4 h annealing at 1600 °C and, (ii) 50 % after a 12 h annealing at 1600 °C.

4.2 UO₂ microstructural changes observed by TEM

4.2.1 Microstructural changes induced by ion implantation

Figure 4 shows a bright field image obtained on the Cs as-implanted sample (fluence of 10^{15} at·cm⁻²) on which the dpa distribution (in red) and the Cs depth profile (in white) calculated by SRIM have been superimposed. Three sharp zones can be distinguished in function of the dark contrast intensity, which indicates different concentrations of visible extended defects. A high concentration of dislocation loops with a size of about 5-10 nm is observed in a zone located between 85 nm and 200 nm (zone 2). Less damage is observed in zone 1 between the surface and a depth of about 85 nm, although this is the region where most dpa are produced by the Cs implantation according to the SRIM calculations. A few small dislocation loops (at most 5 nm in size) remain present in zone 3 with a decreasing density until a depth of around 300 nm. Beyond ~300 nm, the image is identical to the UO₂ virgin sample image (see Figure 2). At last, no precipitation or bubble formation is observed after the implantation of caesium for a fluence of 10^{15} Cs·cm⁻². An accurate quantification has not been made at this stage but the TEM images evidence the difference in dislocation loop density especially following the Cs distribution profile. As an indication, the concentration of loops in zone 1 amounts about 1.2×10^{22} m⁻³ and this value is about 4 times higher in zone 2 whereas it decreases to less than 10^{22} m⁻³ in zone 3.

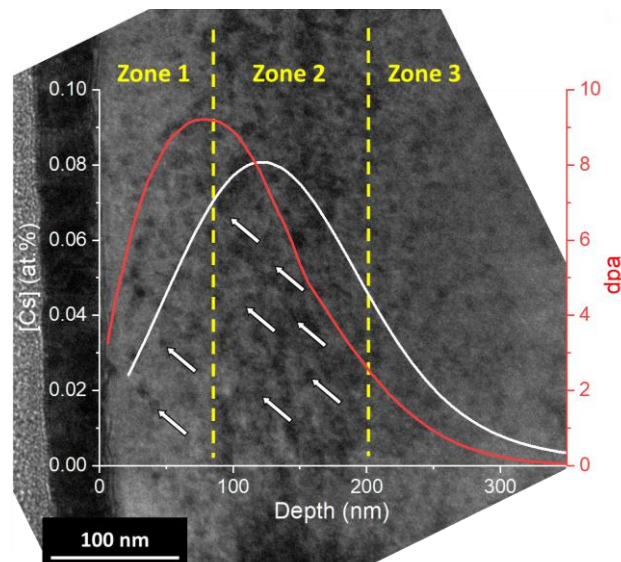


Figure 4- TEM bright field image obtained on the as-implanted sample (fluence of 10^{15} Cs·cm⁻²). The dpa distribution (in red) and the Cs depth profile (in white) as calculated by SRIM are superimposed. Three zones have been delimited with the contrast intensity, which is indicative of the amount of extended defects. White arrows point on some dislocation loops.

4.2.2 Microstructural changes induced by the annealing at 1000 °C

Figure 5 displays the TEM image of a Cs implanted sample after annealing at 1000 °C, in underfocused beam conditions (Figure 5.a) and overfocused beam conditions (Figure 5.b). Changing the focus conditions allows revealing the presence of cavities that appear as white spots in underfocused conditions and as black spots in overfocused conditions. As no Cs release was measured by SIMS, it can be assumed that the cavities are filled with caesium atoms and these objects will be further referred in this paper as “bubbles”. So, nanometric Cs bubbles with a size (referring to their diameter) of (2 ± 0.5) nm are visible from the surface down to a depth of 150 nm. No bubble beyond this depth can be confirmed due to the presence of too many extended defects that can mask the bubbles within our diffraction conditions. In zone 1, a density of $(4.8 \pm 1.3) \times 10^{23}$ bubbles·m⁻³ was determined by counting manually the bubbles on different images from three different areas of the sample.

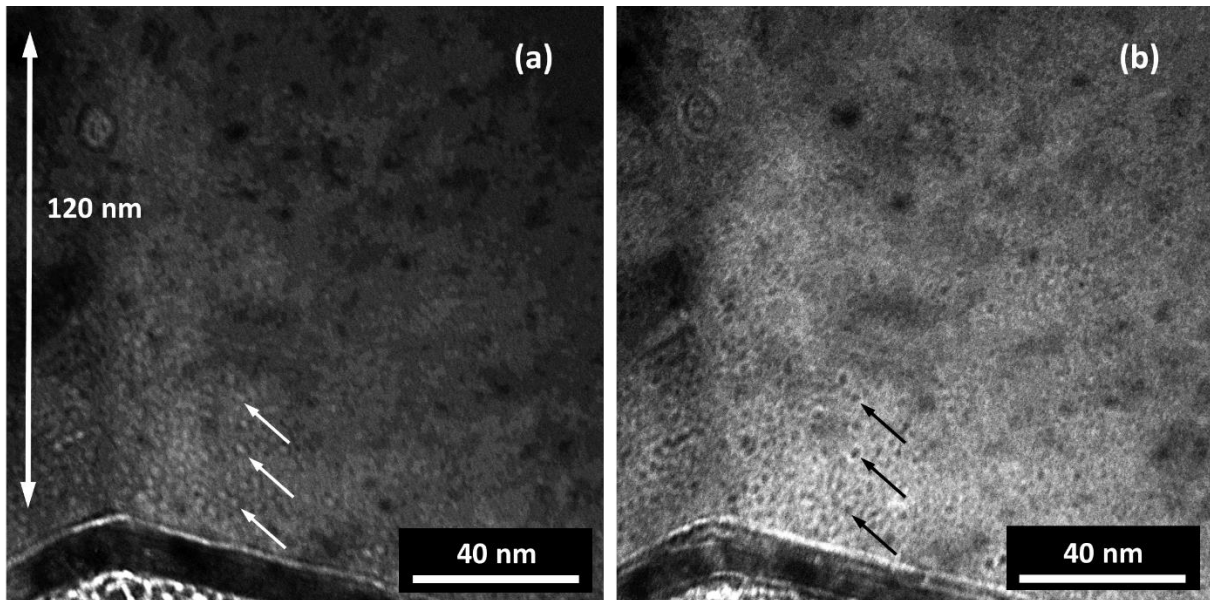


Figure 5- TEM bright field images of UO₂ pellets implanted at a fluence of 10^{15} Cs·cm⁻² and annealed at 1000 °C during 4 h in underfocused beam conditions (a) and in overfocused beam conditions (b). Arrows point at typical bubbles.

Figure 6 displays the combination of the Cs depth profile after annealing at 1000 °C together with a TEM image taken under different conditions (orientation and magnification) than those of Figure 5. We observe three different zones that are delimited by dashed lines in the figure. These zone bounds are roughly the same than the ones seen on the as-implanted sample (see Figure 4). We can also observe that zone 3 seems to host a larger population of extended defects than zone 2, which is a big difference with the as-implanted sample. This could indicate a migration and/or a growth of the dislocation loops which were previously mainly observed in zone 2. The frontier between zone 2 and zone 3, *i.e.* around 200 nm below the surface, contains dislocation lines of larger size than the ones

observed on the as-implanted sample. These defects can be correlated to the shoulder observed on the Cs SIMS profile at around 200 nm. We can therefore assume that the shoulder is consecutive to a local redistribution of Cs atoms along the dislocations. The dislocation loop concentration in zone 3 (Figure 6) has been evaluated to be around $3 \times 10^{22} \text{ m}^{-3}$ with sizes up to 10 nm whereas this concentration drops to $4 \times 10^{21} \text{ m}^{-3}$ in zone 2 and with much smaller loops of 1-2 nm.

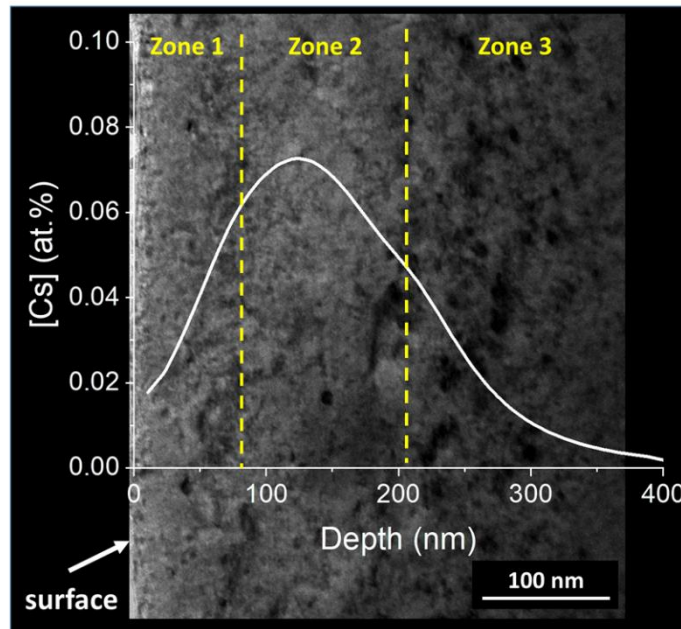


Figure 6- TEM bright field image of UO_2 pellets implanted at a fluence of $10^{15} \text{ Cs} \cdot \text{cm}^{-2}$ and annealed at $1000 \text{ }^\circ\text{C}$ during 4 h with the superimposition of the corresponding SIMS depth profile.

4.2.3 Microstructural changes induced by the annealing at $1600 \text{ }^\circ\text{C}$

Figure 7 presents the TEM images obtained from a Cs sample annealed at $1600 \text{ }^\circ\text{C}$ during 12 h. In Figure 7.a, we observe that no more dislocations appear in the whole Cs implanted region. This result indicates that all the dislocation loops and lines formed by ion implantation have been annealed. Figure 7.b displays the same region but with a magnification allowing a comparison with the Cs profile. A string formed of Cs bubbles of different nature is observed at around 50 nm below the surface. This line of bubbles fits perfectly with the Cs surface peak observed by SIMS on the sample annealed at $1600 \text{ }^\circ\text{C}$. We note two bubble populations according to their size and shape: numerous spherical small bubbles and some polyhedral (faceted) larger bubbles. Figure 8 presents a high magnification TEM micrograph focused on the bubble line (Figure 8.b) with a graph displaying the number of bubbles as a function of their size (Figure 8.a). The histogram was determined by counting bubbles from three different TEM images and was divided by 1 nm bins. It represents a total population of 140 bubbles. Figure 8.a clearly shows the correlation between the bubble shape and size: spherical bubbles have a

size below 5 nm with a distribution maximum located at 3 nm while faceted bubble size ranges between 6 nm and 10 nm. The density of bubbles has been determined as $(6.3 \pm 2.2) \times 10^{22}$ bubbles·m⁻³ for spherical bubbles and $(1.3 \pm 0.7) \times 10^{22}$ bubbles·m⁻³ for faceted bubbles. It could be argued that for the smaller bubbles the spherical nature could be doubtful and is mainly due to the limitation of the out-of-focus limitations whereas for the larger ones the shape is more evident. In their paper, Snoeck *et al.* [33] describe how electron holography can distinguish the faceting. In the discussion here it will be referred as spherical when mentioning the small bubbles and faceted for the larger ones as it is the way they were observed.

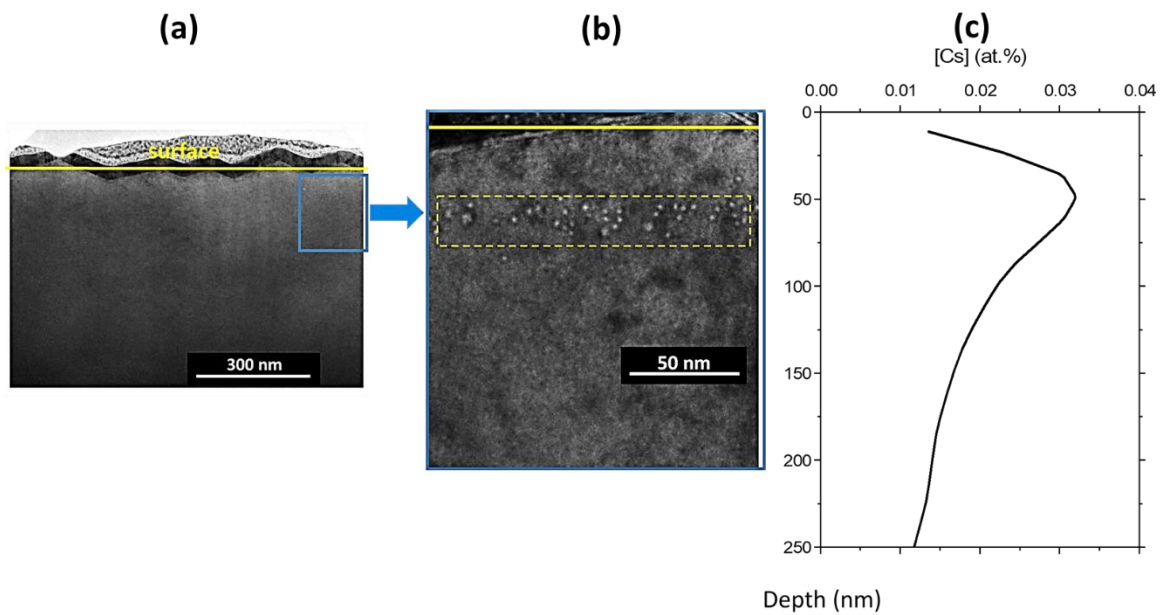


Figure 7- TEM bright field images of: (a) UO₂ pellets implanted at a fluence of 10^{15} Cs·cm⁻² and annealed at 1600 °C during 12 h, (b) the first 200 nm (zoom of the blue rectangle in a) from the surface are displayed at higher magnification, revealing the presence of Cs bubbles parallel to the surface at 50 nm (dashed yellow rectangle). This bubble distribution is correlated with the Cs accumulation at a depth of around 50 nm and visible on the profile as obtained from SIMS measurements and presented in (c).

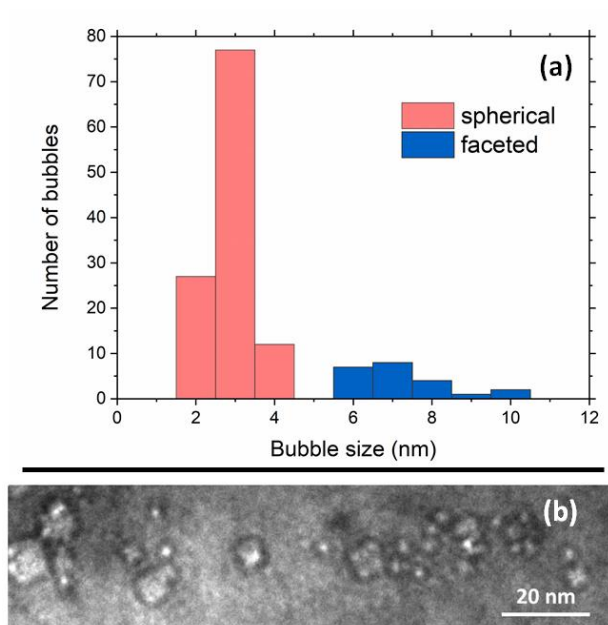


Figure 8- (a) Spherical and faceted caesium bubble size distribution (total population of 140) determined from three different TEM images taken from a UO_2 pellet implanted at a fluence of $10^{15} \text{ Cs}\cdot\text{cm}^{-2}$ and annealed at $1600 \text{ }^\circ\text{C}$ during 12 h. A TEM bright field image of Cs bubbles taken at high magnification is shown in (b).

For comparison with Cs, we have analysed a UO_2 sample implanted with xenon and annealed under the same conditions (implantation fluence of $10^{15} \text{ at}\cdot\text{cm}^{-2}$ and annealed at $1600 \text{ }^\circ\text{C}$ for 12 h). Figure 9 presents one STEM micrograph (Figure 9.a), one TEM image in underfocused conditions (Figure 9.b) and the Xe depth profile measured by SIMS. As for the Cs implanted sample, no dislocations are visible anymore after the $1600 \text{ }^\circ\text{C}$ annealing. The underfocused TEM bright field image in Figure 9.b highlights the contrast of bubbles present in the overall implanted depth, which are also detected in the STEM image. Two populations of spherical bubbles are resolved, the size of which is respectively of 1-3 nm and 5-7 nm. The density of the Xe bubble population has been determined to be in the range of $5\text{-}9 \times 10^{22} \text{ bubbles}\cdot\text{m}^{-3}$, which is of the same order of magnitude than the one measured on the caesium implanted sample and annealed at $1600 \text{ }^\circ\text{C}$.

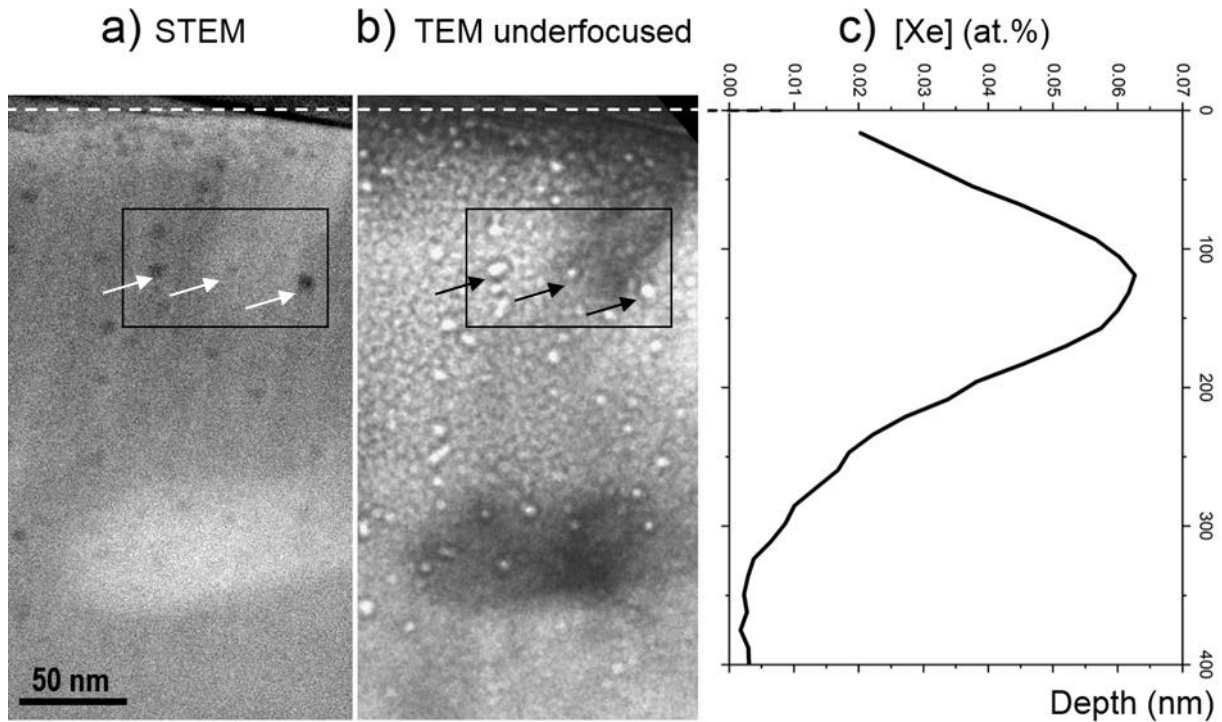


Figure 9- STEM (a) and underfocused TEM bright field (b) micrographs of the same sub-surface area of a UO_2 sample implanted in Xe at a 10^{15} $\text{at}\cdot\text{cm}^{-2}$ fluence and annealed at 1600°C for 12 hours. Dark frames identify the same bubbles and arrows point to some of them particularly. Xe depth profile measured by SIMS is shown in (c).

5. Discussion

In order to help the discussion, table 2 gathers the main TEM observations of the samples implanted with Cs or Xe and subsequently annealed at 1000°C or 1600°C .

Table 2- Main results obtained by TEM on samples implanted with Cs or Xe (10^{15} $\text{at}\cdot\text{cm}^{-2}$) and subsequently annealed (1000°C or 1600°C).

Annealing conditions	Caesium		Xenon
	1000°C (4h)	1600°C (12h)	1600°C (12h)
Bubble populations	1	2	2
Bubble shape	Spherical	Spherical and faceted	Spherical
Bubble mean size (nm)	2 ± 0.5	3 ± 1 and 8 ± 2	2 ± 1 and 6 ± 1
Bubble density (m^{-3})	$(4.8 \pm 1.3) \times 10^{23}$	$(6.3 \pm 2.2) \times 10^{22}$ and $(1.3 \pm 0.7) \times 10^{22}$	$5\text{-}9 \times 10^{22}$

The competition between trapping and diffusion of volatile atoms such as caesium and xenon is mainly governed by the quantity, the nature and the mobility of the defects present in UO_2 . It is therefore of primary importance to characterise first the ion implantation induced defects.

5.1 Defects created during ion implantation at room temperature (RT)

TEM examinations performed on Cs as-implanted samples show mostly dislocations with a size between 5 and 10 nm. These results are consistent with those reported in the literature especially the work of Sabathier *et al.* [34] who observed by TEM the nucleation of Cs and Xe bubbles implanted in UO₂ at low temperature (600 °C and below). They observed 7 nm dislocation loops after 300 keV Cs implantation in UO₂ at a fluence of 5×10^{14} at·cm⁻² (maximum concentration of 0.4 at. %) and also reported the presence of some dislocation lines at a fluence of 10^{15} at·cm⁻² [34]. For xenon implantation at a fluence of 5×10^{14} ions·cm⁻² in UO₂, two studies can be benchmarked with ours. In the first one, He *et al.* report dislocations formation with a size of about 7 nm and a density of 2.5×10^{22} m⁻³ [32]. In the second study, Onofri *et al.* show that a 5×10^{14} at·cm⁻² fluence for Xe implantation produces almost exclusively (1.4×10^{22} m⁻³) of large (~11 nm) dislocation loops and some few (1.2×10^{15} m⁻³) dislocation lines [35]. We can therefore conclude that, for comparable implantation conditions, the damage and extended defect formation are nearly the same after Cs implantation and after Xe implantation. These kind of defects created by ion implantation correspond also to the ones observed during reactor operation in a fuel irradiated at a low burnup and at RT [36]. In our experiments, the dislocations are mainly observed between 85 nm and 200 nm below the surface because of the displacement cascades occurring at the end of the Cs or Xe atoms implantation range. The defect formation process can be described in atomic scale simulation by classical molecular dynamics (MD) like for example in [37]. In this work, the formation of vacancy clusters was shown in the cascade displacement core whereas the formation of interstitial clusters was foreseen in the cascade periphery. This is explained by the dislocation punching due to the elastic wave produced during a thermal spike phase, the interstitials being essentially produced at the interface between the “molten region” and the solid matrix. In addition, the same authors in [38] have highlighted that an increase of temperature favours the formation of clustered interstitial defects until the formation of dislocation lines. This is in agreement with the present experimental results. Indeed dislocation lines are barely observed on the Cs as-implanted sample whereas they are clearly seen at a depth of about 200 nm in the Cs-implanted sample annealed at 1000 °C. The local atomic redistribution occurring during their formation is probably responsible for the slight increase of Cs concentration observed at the same depth on the SIMS profile.

Another feature regarding the observations made on the as-implanted sample is that no Cs bubbles were visible. A general statement is that bubbles nucleate easier with increasing temperature and increasing implantation fluence. Except the work of He *et al.* [32] which highlights 1.9 nm xenon bubbles for samples implanted at 5×10^{14} ions·cm⁻² at RT (but without considering a possible sample heating by the beam), a minimum temperature of 100 °C is required to observe xenon bubbles in UO₂

[39]. The presence of xenon bubbles at RT would indicate a direct nucleation at vacancy clusters or through a ballistic process that does not require thermal Xe diffusion.

5.2 Nucleation of bubbles after annealing at 1000 °C

At 1000 °C, nanometer size bubbles of caesium atoms are observed from the surface down to a depth of around 100 nm but most probably these bubbles are present all along the implantation depth, forming a trap for caesium. This explains that no Cs diffusion nor volatilization was detected at this temperature. The formation of Cs bubbles was already observed in the work of Sabathier *et al.* [34]. They studied UO₂ implanted with caesium at a maximum concentration of 2 at. % (fluence of 10^{16} ions·cm⁻²) and annealed at 600 °C. They reported bubbles with size around 1.7 nm and a density of $(10 \pm 5) \times 10^{23}$ bubbles·m⁻³. The size value and the density value are pretty close to ours even if the concentration of caesium is 25 times greater in the work of Sabathier *et al.* This could indicate that a saturation threshold for the bubble density is already reached for a fluence of 10^{15} at·cm⁻². The same phenomenon is reported for the xenon implantation in UO₂ in the work of Michel *et al.* [40]. They have varied the implantation fluence and studied bubble formation. They have shown that the bubble size was nearly the same (around 2 nm) whatever the fluence and that the bubble density was increasing with the fluence up to a threshold of around 5×10^{14} at·cm⁻².

Moreover, the comparison with the work of Sabathier *et al.* [34] highlights the strong influence of the Cs (or Xe) concentration and of the annealing temperature on the bubble nucleation. For a maximum concentration of 2 at. %, bubble precipitation was observed at 400 °C for xenon and at 500 °C for caesium. For a maximum concentration of 0.4 at. %, xenon bubbles appear at 600 °C. In our experiment, for a maximum concentration of 0.08 at. %, we observed caesium bubbles at 1000 °C. So, at “low” temperatures (below 1000 °C), it seems that xenon and caesium implanted at the same concentration behave the same way, *i.e.* both elements form spherical bubbles in UO₂ with similar size, density and threshold temperature for nucleation. These bubbles are also probably pressurized if we refer to the papers of Martin *et al.* [41-42]. They have shown by X-Ray absorption spectroscopy that Xe nanobubbles remain highly pressurized at roughly 2.0 GPa after an 800 °C annealing of a UO₂ sample implanted with Xe at a concentration of around 8 at. %. However, the concentration is one hundred times higher than in the present experiment which could modify the quantity and the nature of the defects trapping the volatile atoms.

One way to better understand the trapping of xenon and caesium into defect clusters is to perform atomic scale simulations. Indeed, bubble nucleation is associated with the formation of vacancy

clusters in which atoms are incorporated as shown by MD simulations [37]. Yun *et al.* [43] used *ab initio* calculations to obtain the incorporation energy of xenon in different point defects. They have evidenced that the Schottky defect (two oxygen vacancies bound to a uranium vacancy) is the most stable position for xenon. Andersson *et al.* [44] have calculated a low Xe incorporation energy of 0.18 eV for this defect. Also, from a MD study, Murphy *et al.* [45] have shown that xenon is very stable in nanovoids (created from several Schottky defects) for temperatures up to 1050 K (780 °C) and that no thermal resolution occurs during the simulation time. Not so far from these insights, Moore *et al.* [46] have found by MD simulations that in the context of a vacancy-saturated model, the formation of stable Xe clusters, driven by the migration of Xe atoms by vacancy-assisted diffusion, was possible. For caesium, only a few data exists in literature. Gupta *et al.* [47] have shown that caesium can be incorporated with a similar negative energy (~ -1 eV) into a uranium vacancy, a divacancy (uranium vacancy bound to an oxygen vacancy) or a Schottky defect. All these defects involving a uranium vacancy can constitute a nucleation centre from which a bubble can grow with further trapping of caesium atoms. So whereas xenon can be only incorporated into Schottky defects and has a tendency to form clusters, caesium might be incorporated in smaller defects and its incorporation energy remains favourable (even if not so much) in any uranium defect type. To sum up, literature results seem to indicate that the nature and consequently the sink strength of the caesium traps might be different from the xenon ones.

5.3 Growth of bubbles and mobility of caesium and xenon at 1600 °C

Results obtained from 1600 °C annealing of implanted UO₂ pellets show a different behaviour between xenon and caesium. Our similar conditions of implantation and annealing allow a direct comparison of the two elements. This is particularly relevant as it is often assumed that caesium behaves like rare gases in UO₂ above 1200 °C, the threshold temperature value to form gaseous caesium according to Walker *et al.* [12]. In our experimental conditions, no significant release or diffusion of Xe could be evidenced while a significant release of Cs was evidenced: 50 % of Cs is released after a 12 h annealing, the remaining part either accumulating at the surface or diffusing into the bulk. The difference of release rate between caesium and xenon is likely due to different growth kinetics and behaviour of bubbles. TEM characterisations give insights into the different bubble growth mechanisms for caesium and xenon. We observe, in Figure 8, the presence of several Cs spherical bubbles with a size ranging between 1.5 nm and 4.5 nm (taking into account the error bars). It seems that there is only one distribution centred at around 3 nm. Figure 9 displays two Xe spherical bubble populations with a size centred at 2 nm and 6 nm. The Xe bi-population is not a surprise and was already reported by Chkuaseli and Matzke [48] at a xenon concentration of 0.01 at. % in UO₂ and by Martin *et al.* [41] at a xenon

concentration of 8 at. % in UO_2 after annealing at 1500 °C. In most materials, bubbles growth begins noticeably when thermal vacancies are significantly available, which is the case at 1600 °C. Further growth can then occur by migration-coalescence and even more in a vacancy gradient process as it was proposed by Evans [49]. In our experiments, we can assume that the source of the vacancy flux originates from the surface as xenon or caesium atoms are implanted in the first 300 nm below the surface. The bubble migration velocity can be estimated from the calculations of Veshchunov *et al.* [50]. According to these authors, the mobility of Xe bubbles increases with the temperature and is maximum for bubbles with a radius of 2 nm. They have shown that this mobility decreases with the increase of the bubble size. Veshchunov calculated a diffusivity coefficient “D” at 1800 K (1525 °C) for a bubble radius of 1 nm (which means a size of 2 nm) of $10^{-20} \text{ m}^2 \text{ s}^{-1}$. We can thus estimate a diffusion length ($\sim\sqrt{Dt}$) during a four hour annealing time (“t”) of 12 nm. This indicates that bubbles in a close vicinity can easily coalesce under our conditions of annealing. The Evans process can explain the growth of the spherical bubbles for caesium and for xenon in UO_2 at 1600 °C. However, no bi-population of Cs bubbles is observed and the maximum size is lower than for xenon. This indicates that the bubble growth is different and that other mechanisms occur at the same time for caesium in UO_2 . For example in [45], Murphy *et al* suggested a bubble growth by displacements of oxygen near the bubble surface rather than by U vacancies absorption.

We will now highlight the two main differences noted between the behaviour of xenon and of caesium at 1600 °C.

The first one concerns the regions where the bubbles are located. While we can observe xenon bubbles in the whole implantation region, caesium bubbles are only present inside a limited band centred at around 50 nm below the surface with a width of around 40 nm. In the rest of the sample, no caesium bubbles are observed. In particular, no Cs bubbles are visible in the first 30 nm below the surface. One hypothesis to explain this result is to consider bubble diffusion towards the surface. Verma *et al.* numerically addressed the migration of the fission gas bubbles in [51] and showed that the influx of vacancies from the surface towards the bulk would create a vacancy concentration gradient. The consequence is a directed diffusion of bubbles towards the surface accelerating the release of the gas. In the present experiment, this assumption is only valid if we consider that the diffusion coefficient of Cs bubbles is higher than the Xe bubble one. Indeed, no release of xenon is measured and we can observe small Xe bubbles pinpointed really close to the surface as shown in Figure 9 whereas 50 % of caesium is released from UO_2 sample surface.

Another hypothesis to explain the disappearance of caesium bubbles near the surface and in the bulk of our samples is to consider the thermal resolution of caesium atoms into the UO_2 matrix. Of course, such a process is related to the atomic solubility in UO_2 . Xenon is considered as insoluble in UO_2 , so its

thermal resolution is highly unlikely even at high temperature. As already pointed out in the 5.2 paragraph, an indicator of this low solubility is shown by the value of incorporation energies which remain always positive whatever the Xe location. This is also consistent with the simulations performed by Murphy *et al.* [45] already previously mentioned. Xe thermal resolution would be possible only for highly over pressurized bubbles (very high temperature and high Xe content or very quick temperature transient) which was not achieved in our experiment. Caesium is not insoluble in UO₂ but has a low solubility. The Cs incorporation energy remains always slightly negative for Cs in uranium vacancies as shown by electronic structure simulations [47] or even more indirectly by empirical interatomic potential simulations [52]. In addition, Walker *et al.* [53] have estimated a solubility below 0.06 wt % (~0.01 at. %) at 1700 °C. This value corresponds roughly to the concentration of caesium in the rear part of the as-implanted profile. Moreover, it is worth noting that the annealing of dislocations was observed in alpha-damaged (U, Pu)O₂ samples annealed at 1800 K (1523 °C) [54].

To sum up, Cs atomic thermal resolution can be enhanced by the vacancies created by the ion implantation, by the surface but also by those created by the annealing of the dislocations at 1600 °C. Finally, the mechanism formation of the specific region with Cs bubbles can be illustrated using

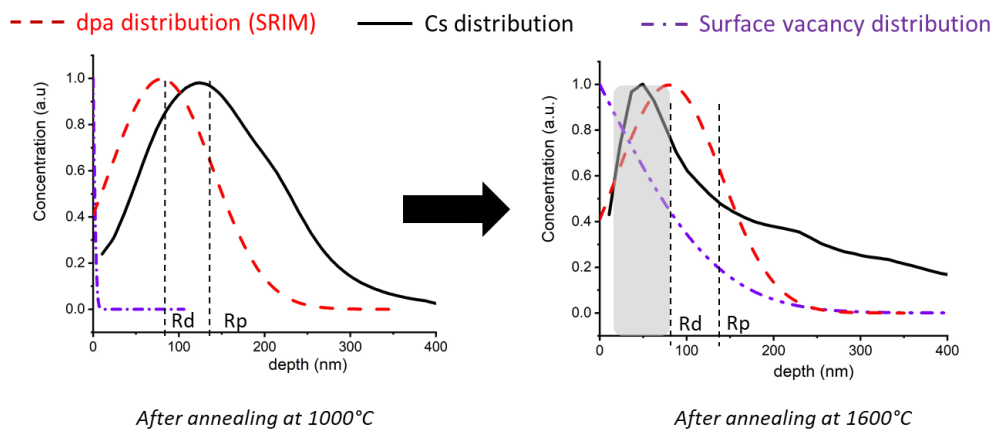


Figure 10. This figure displays the distributions of the defects which can be involved in the formation and migration of the caesium bubbles. The quantity of defects being unknown after annealing, the distributions have been normalized to one. The dpa distribution stands for the defects created by implantation as calculated by SRIM. Even if the distribution evolves after annealing, it gives an estimate of the presence of the implantation defects. The surface vacancy distribution has been represented by the function expressed in (eq. 2).

$$C(x, t) = \operatorname{erfc}\left(\frac{x}{2\sqrt{Dt}}\right) \quad (\text{eq. 2})$$

With: x , the depth

D , the diffusion coefficient of vacancies close to the surface

t , the time of annealing

The distribution was drawn at 1000 °C taking a constant for the \sqrt{Dt} term. The distribution at 1600 °C has been calculated with the ratio $D_{1600^\circ\text{C}}/D_{1000^\circ\text{C}}$ thanks to the Arrhenius law (eq. 3). This allows a rough idea of the depth reached by the surface vacancies.

$$\frac{D_{1600^\circ\text{C}}}{D_{1000^\circ\text{C}}} = \exp\left(-\frac{E_a}{1873 \cdot k_B} + \frac{E_a}{1273 \cdot k_B}\right) \quad (\text{eq. 3})$$

With: E_a , the activation energy for the cation surface vacancies. A value of 3.0 eV has been chosen from molecular dynamics calculations [55]

k_B , the Boltzmann constant ($8.62 \times 10^{-5} \text{ eV} \cdot \text{K}^{-1}$)

At 1000 °C, only spherical bubbles ($\sim 2 \text{ nm}$) are visible down to a depth corresponding roughly to the projected range (R_p) of the Cs distribution and the surface vacancy gradient is limited. After the annealing at 1600 °C, thermal resolution occurs in the whole sample. This favours the disappearance of the small-pressurised bubbles and a Cs atomic diffusion towards the surface. At the same time, because of the vacancies influx from the surface, caesium is trapped in a region at a depth of around 50 nm (with a width of $\pm 20 \text{ nm}$) where two different defect gradients coexist. The bubbles are visible down to a depth corresponding roughly to the maximum of the dpa distribution (R_d) calculated by SRIM. Near the surface (the first twenty nanometers), the diffusion of small bubbles enhanced towards the surface added to the thermal resolution explain the disappearance of the Cs bubbles.

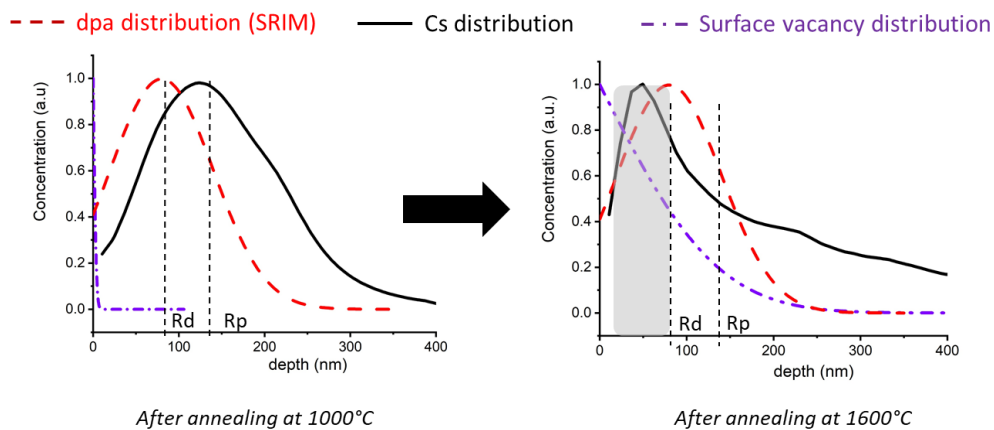


Figure 10- Sketch of the formation of the specific region (grey zone) where Cs bubbles develop after annealing at 1600 °C. R_d stands for the range of the dpa distribution calculated by SRIM and R_p for the projected range of the Cs distribution

The second difference between xenon and caesium behaviour at 1600 °C concerns the bubble growth evolution. While Xe bubbles remain with a quite spherical shape, we observe large ($\sim 10 \text{ nm}$) faceted Cs bubbles in the region described previously. One can consider that, during the 1600 °C annealing,

some Cs atoms might be re-soluted from bubbles and made available for diffusion. In a second phase, they could either be released or be trapped into already existing bubbles or into nanovoids created during implantation, thus stopping their diffusion. Rest *et al.* [56] have calculated that resolution probability for 100 nm radius bubbles was 40 times lower than for 3 nm bubbles. This would indicate that the small spherical bubbles present near larger ones would dissolve into the UO₂ matrix at a much higher rate than the larger ones. These large bubbles will incorporate more Cs atoms and vacancies explaining their size increase and the evolution of their shape that becomes faceted. This mechanism, which implies that a system constituted of different bubble size tends to a more energetically favourable state promoted by a decrease of its interface energy, is known as the Ostwald ripening mechanism. As a summary, Figure 11 illustrates the Cs bubble nucleation and growth in UO₂ during annealing. Such bubble growth was also reported in [57] for the 1.5 MeV Kr implantation at the very high fluence of 5×10^{16} ions·cm⁻². The authors have indicated the formation, after annealing at 1000 °C, of bubbles of around 1.5 nm in size. After annealing at 1300 °C (~1 hour) the bubble size distribution was no longer uniform and some large bubbles (several nm in diameter) appeared, some of them exhibiting facets that correspond to the (111) and (020) planes of UO₂. They also reported an increase of the number of the faceted bubbles at 1600 °C. This means that, likely, a coarsening of the spherical bubbles occurred as well as an increase of the number of faceted bubbles.

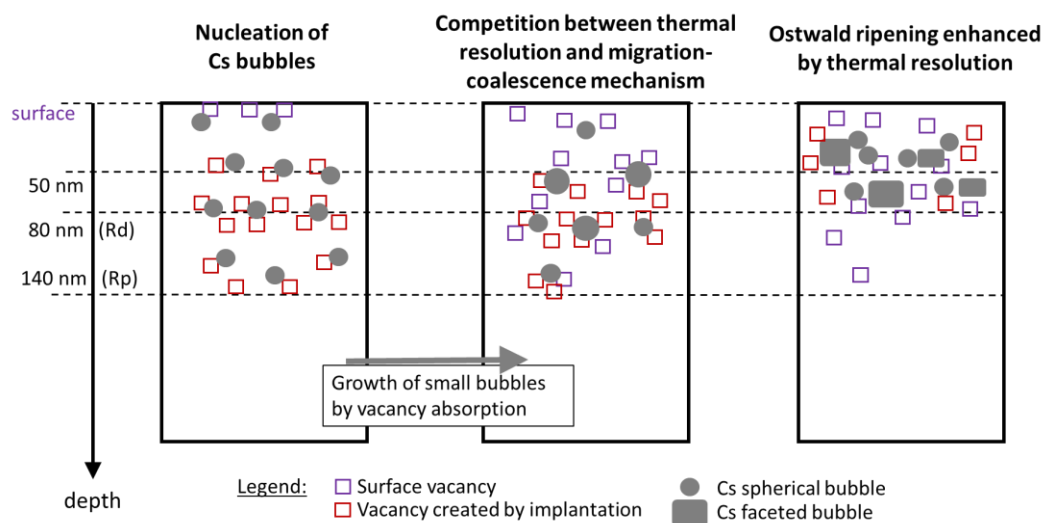


Figure 11- Schematic illustration of the different mechanisms of the Cs bubble nucleation and growth

From all these results, we can conclude that Xe being insoluble in UO₂, the thermal resolution is highly unlikely and therefore the growth of xenon bubbles through the Ostwald ripening mechanism has a low probability to happen. However, solubility can be enhanced by defect concentration and temperature. Depending on the nature of the volatile species, thermal resolution is also a process to consider which

will determine the thermal behaviour of these species either on the growth of the bubbles or on the release of the gas.

6. Conclusions

This paper compares the thermal migration of caesium and xenon implanted in UO_2 at a fluence of $10^{15} \text{ Cs}\cdot\text{cm}^{-2}$. The originality of the work was to characterise Cs and Xe behaviour after annealing at 1000 °C and 1600 °C by combining SIMS depth profiles with TEM examinations. Caesium is known to be a volatile species and its migration is often compared to the xenon migration.

1000 °C is the typical temperature at the centre of a UO_2 pellet under normal reactor operation. No Cs release is observed after a 4 h annealing at this temperature. This is explained by the formation of nanometric bubbles (diameter of around 2 nm), the nucleation mechanism of which seems to be similar to the xenon one.

At high temperature (1600 °C), caesium and xenon exhibit a different behaviour, which can be explained by their respective solubility and thermal resolution in UO_2 . On one hand, xenon atoms remain trapped into bubbles divided into two populations with a mean size of respectively 2 and 6 nm. On the other hand, an important release of Cs was measured (50 % after 12 h of annealing) and two kinds of bubbles (3 nm spherical bubbles and 8 nm faceted bubbles) are observed in a band located at a depth of around 50 nm from the surface.

One assumption to explain the growth of the spherical bubbles (especially Xe bubbles) is the Evans (migration coalescence) mechanism. The fraction of Cs bubbles, which are bigger and faceted, probably results from Ostwald ripening.

It can be concluded that the main parameters governing the stability of bubbles and their growth kinetics are the availability of thermal vacancies in conjunction with the threshold temperature for the thermal resolution. Other TEM examinations performed on samples annealed at intermediate temperatures (between 1000 °C and 1600 °C) are therefore planned in order to identify the threshold temperature of caesium thermal resolution and the first steps of the caesium diffusion.

Acknowledgements

The authors wish to express their thanks to Anthony Duranti (IP2I Lyon, France) for the Cs implantation on the IMIO400 implanter and Dr. Philippe Sainsot for interferometry measurements (INSA Lyon, France). Special thanks are also addressed to Alessandro Benedetti (JRC Karlsruhe, Germany) for the optimum FIB lamellae preparation and for the TEM examinations. Thanks to the InnoEnergy PhD

School Programme and the European Institute of Technology (EIT) for the financial support to go to the JRC in Karlsruhe.

References

- [1] D. Champion, I. Korsakissok, D. Didier, A. Mathieu, D. Quelo, J. Groell, E. Quentric, M. Tombette, JP. Benoit, O. Saunier, V. Parache, M. Simon-Cornu, MA. Gonze, B. Cessac, E. Navarro, AC. Servant-Perrier, « *The IRSN's earliest assessments of the Fukushima accident's consequences for the terrestrial environment in Japan* », Radioprotection 48 (2013) 11–37. DOI: [10.1051/radiopro/2012052](https://doi.org/10.1051/radiopro/2012052)
- [2] Clefs CEA n°53, « *Déchets radioactifs, des solutions en progrès continu* » (2005) ISSN 0298-6248.
- [3] R.J.M. Konings, T. Wiss, O. Beneš, « *Predicting material release during a nuclear reactor accident* », Nature Mater. 14 (2015) 247-252. DOI: [10.1038/nmat4224](https://doi.org/10.1038/nmat4224)
- [4] Y. Pontillon and G. Ducros, « *Behaviour of fission products under severe PWR accident conditions The VERCORS experimental programme-Part 2: Release and transport of fission gases and volatile fission products* », Nucl. Eng. Des. 240 (2010) 1853-1866. DOI: [10.1016/j.nucengdes.2009.06.024](https://doi.org/10.1016/j.nucengdes.2009.06.024)
- [5] T. Kudo, M. Kida, T. Nakamura, F. Nagase, T. Fuketa, « *Releases of cesium and poorly volatile elements from UO₂ and MOX fuels under severe accident conditions* », J. Nucl. Sci. and Technol. 44 (2007) 1421-1427. DOI: [10.3327/jnst.44.1421](https://doi.org/10.3327/jnst.44.1421)
- [6] M. Schwarz, G. Hache, P. von der Hardt, « *PHEBUS FP: A severe accident research programme for current and advanced light water reactors* », Nucl. Eng. Des. 187 (1999) 47-69. DOI: [10.1016/S0029-5493\(98\)00257-X](https://doi.org/10.1016/S0029-5493(98)00257-X)
- [7] M. Peehs, G. Kaspar, KH. Neeb, « *Cs and I-release source terms from irradiated LWR fuel* », J. Nucl. Mater. 119 (1983) 284-290. DOI: [10.1016/0022-3115\(83\)90205-2](https://doi.org/10.1016/0022-3115(83)90205-2)
- [8] NS. Shcherbina, N. Kivel, I. Gunther-Leopold, « *Effect of Redox Conditions on the Fission Products Release from Irradiated Oxide Fuel* », Procedia Chem. 7 (2012) 104-109. DOI: [10.1016/j.proche.2012.10.019](https://doi.org/10.1016/j.proche.2012.10.019)
- [9] J.-P. Hiernaut, T. Wiss, J.-Y. Colle, H. Thiele, C.T. Walker, W. Goll, R.J.M. Konings, « *Fission product release and microstructure changes during laboratory annealing of a very high burn-up specimen* », J. Nucl. Mater. 377 (2008) 313-324. DOI: [10.1016/j.jnucmat.2008.03.006](https://doi.org/10.1016/j.jnucmat.2008.03.006)
- [10] J.-P. Hiernaut, T. Wiss, D. Papaioannou, R.J.M. Konings, V.V. Rondinella, « *Volatile fission product behavior during thermal annealing of irradiated UO₂ fuel oxidized up to U₃O₈* », J. Nucl. Mater. 372 (2008) 215-225. DOI: [10.1016/j.jnucmat.2007.03.174](https://doi.org/10.1016/j.jnucmat.2007.03.174)
- [11] SG. Prussin, DR. Olander, WK. Lau, L. Hansson, « *Release of fission-products (Xe, I, Te, Cs, Mo and Tc) from polycrystalline UO₂* », J. Nucl. Mater. 154 (1988) 25-37. DOI: [10.1016/0022-3115\(88\)90115-8](https://doi.org/10.1016/0022-3115(88)90115-8)
- [12] CT. Walker, W. Goll, T. Matsumura, « *Further observations on OCOM MOX fuel: Microstructure in the vicinity of the pellet rim and fuel-cladding interaction* », J. Nucl. Mater. 228 (1996) 8-17. DOI: [10.1016/S0022-3115\(97\)00009-3](https://doi.org/10.1016/S0022-3115(97)00009-3)
- [13] E. Geiger, C. Guéneau, Y. Pontillon, EC. Corcoran, « *Modelling nuclear fuel behaviour with TAF-ID: Calculations on the VERDON-1 experiment, representative of a nuclear severe accident* », J. Nucl. Mater. 522 (2019) 294-310. DOI: [10.1016/j.jnucmat.2019.05.027](https://doi.org/10.1016/j.jnucmat.2019.05.027)
- [14] L. Desgranges, C. Riglet-Martial, I. Aubrun, B. Pasquet, I. Roure, J. Lamontagne, T. Blay, « *Evidence of tellurium iodide compounds in a power-ramped irradiated UO₂ fuel rod* », J. Nucl. Mater. 437 (2013) 409-414. DOI: [10.1016/j.jnucmat.2013.02.05](https://doi.org/10.1016/j.jnucmat.2013.02.05)
- [15] L. Desgranges, J. Lamontagne, C. Riglet-Martial, T. Blay, « *Experimental evidence of the formation of a new chemical phase in a power ramped UO₂ nuclear fuel* », J. Nucl. Mater. 457 (2015) 246-251. DOI: [10.1016/j.jnucmat.2014.11.070](https://doi.org/10.1016/j.jnucmat.2014.11.070)
- [16] A.H. Booth, « *A method of calculating fission gas diffusion from UO₂ fuel and its application to the X-2-f loop test* », report CRDC n° 721 (1957).
- [17] WH. Hocking, RA. Verrall, I.J. Muir, « *Migration behaviour of iodine in nuclear fuel* », J. Nucl. Mater. 384 (2001) 45-52. DOI: [10.1016/S0022-3115\(01\)00447-0](https://doi.org/10.1016/S0022-3115(01)00447-0)

- [18] M. Saïdy, W. H. Hocking, J. F. Mouris, P. Garcia, G. Carlot, B. Pasquet, « *Thermal diffusion of iodine in UO_2 and UO_{2+x}* », J. Nucl. Mater. 372 (2008) 405–415. DOI: [10.1016/j.jnucmat.2007.03.272](https://doi.org/10.1016/j.jnucmat.2007.03.272)
- [19] Y. Pípon, N. Toulhoat, N. Moncoffre, H. Jaffrezic, S. Gavarini, P. Martin, L. Raimbault, AM. Scheidegger, « *Thermal diffusion of chlorine in uranium dioxide* », Radiochim. acta 94 (2006) 705-711. DOI: [10.1524/ract.2006.94.9.705](https://doi.org/10.1524/ract.2006.94.9.705)
- [20] L. Sarrasin, C. Gaillard, C. Panetier, Y. Pípon, N. Moncoffre, D. Mangin, R. Ducher, R. Dubourg, « *Effect of the Oxygen Potential on the Mo Migration and Speciation in UO_2 and UO_{2+x}* », Inorg. Chem. 58 (2019) 4761-4773. DOI: [10.1021/acs.inorgchem.8b03076](https://doi.org/10.1021/acs.inorgchem.8b03076)
- [21] S. Portier, S. Brémier, R. Hasnaoui, O. Bildstein, CT. Walker, « *SIMS analysis of ^{83}Kr implanted UO_2* », Applied Surface Science 255 (2008) 1323-1326.
- [22] T. Zweifel, N. Valle, C. Grygiel, I. Monnet, L. Beck, W. Petry, « *Kr implantation into heavy ion irradiated monolithic UeMo/Al systems: SIMS and SEM investigations* », J. Nucl. Mater. 470 (2016) 251-257.
- [23] B. Marchand, N. Moncoffre, Y. Pípon, C. Garnier, N. Béreard, C. Delafoy, M. Fraczkiewicz, A. Perrat-Mabillon, L. Raimbault, P. Sainsot, N. Toulhoat, « *Xenon migration in UO_2 : A SIMS study* », Prog. Nucl. Energ. 57 (2012) 145-149. DOI: [10.1016/j.pnucene.2011.10.009](https://doi.org/10.1016/j.pnucene.2011.10.009)
- [24] N. Djourelou, B. Marchand, H. Marinov, N. Moncoffre, Y. Pípon, P. Nedelec, N. Toulhoat, « *Variable energy positron beam study of Xe-implanted uranium oxide* », J. Nucl. Mater. 432 (2013) 287–293. DOI: [10.1016/j.jnucmat.2012.07.035](https://doi.org/10.1016/j.jnucmat.2012.07.035)
- [25] JF. Ziegler, J.P. Biersack, U. Littmark, *The Stopping and Range of Ions in Solids*, New York, 1985.
- [26] J. Soullard, « *High-voltage electron-microscope observations of UO_2* », J. Nucl. Mater. 135 (1985) 190-196. DOI: [10.1016/0022-3115\(85\)90077-7](https://doi.org/10.1016/0022-3115(85)90077-7)
- [27] L. Desgranges, B. Pasquet, « *Measurement of xenon in uranium dioxide (UO_2) with SIMS* », Nucl. Inst. Met. Phys. Res. B. 215 (2004) 545-551. DOI: [10.1016/j.nimb.2003.08.033](https://doi.org/10.1016/j.nimb.2003.08.033)
- [28] RG. Wilson, « *SIMS Quantification in Si, GaAs, and diamond- an update* », J. Mass Spectrometry. Ion Proc. 143 (1995) 43-49. DOI: [10.1016/0168-1176\(94\)04136-U](https://doi.org/10.1016/0168-1176(94)04136-U)
- [29] B. Marchand (2012), PhD thesis : « *Effets de la température et de l'irradiation sur la mobilité du xénon dans UO_2 : étude profilométrique et microstructurale* ». Université Claude Bernard - Lyon I, France. tel-00830100.
- [30] P. Peres, S. Choi, F. Desse, P. Bienvenu, I. Roure, Y. Pípon, C. Gaillard, N. Moncoffre, L. Sarrasin, D. Mangin, « *Dynamic SIMS for materials analysis in nuclear science* », J. Vac. Sci. & Tech. B 36 (2018) 03F117. DOI: [10.1116/1.5017027](https://doi.org/10.1116/1.5017027)
- [31] T. Wiss, H. Thiele, A. Janssen, D. Papaioannou, VV. Rondinella, and RJM. Konings, « *Recent Results of Microstructural Characterization of Irradiated Light Water Reactor Fuels using Scanning and Transmission Electron Microscopy* », JOM. 64 (2012) 1390-1395. DOI: [10.1007/s11837-012-0483-1](https://doi.org/10.1007/s11837-012-0483-1)
- [32] L. He, J. Pakarinen, M.A. Kirk, J. Gan, A.T. Nelson, X.-M. Bai, A. El-Azab, T.R. Allen, « *Microstructure evolution in Xe-irradiated UO_2 at room temperature* », Nucl. Inst. Meth. Phys. Res. B 330 (2014) 55-60. DOI: [10.1016/j.nimb.2014.03.018](https://doi.org/10.1016/j.nimb.2014.03.018)
- [33] E. Snoeck, J. Majimel, M.O. Ruault, M. J. Hýtch, « *Characterization of helium bubble size and faceting by electron holography* », J. Appl. Phys. 100 (2006) 023519. DOI: [10.1063/1.2216791](https://doi.org/10.1063/1.2216791)
- [34] C. Sabathier, L. Vincent, P. Garcia, F. Garrido, G. Carlot, L. Thomé, P. Martin, C. Valot, « *In situ TEM study of temperature-induced fission product precipitation in UO_2* », Nucl. Inst. Meth. Phys. Res. B 266 (2008) 3027-3032. DOI: [10.1016/j.nimb.2008.03.158](https://doi.org/10.1016/j.nimb.2008.03.158)
- [35] C. Onofri, C. Sabathier, C. Baumier, C. Bachelet, H. Palancher, B. Warot-Fonrose, M. Legro, « *Influence of exogenous xenon atoms on the evolution kinetics of extended defects in polycrystalline UO_2 using in situ TEM* », J. Nucl. Mater. 512 (2018) 297-306. DOI: [10.1016/j.jnucmat.2018.10.025](https://doi.org/10.1016/j.jnucmat.2018.10.025)
- [36] AD. Whapham, BE. Sheldon, « *Radiation damage in uranium dioxide* », Philos. Mag. 12 (1965) 1179-1192. DOI: [10.1080/14786436508228669](https://doi.org/10.1080/14786436508228669)

- [37] G. Martin, P. Garcia, C. Sabathier, L. Van Brutzel, B. Dorado, F. Garrido, S. Maillard, « *Irradiation-induced heterogeneous nucleation in uranium dioxide* », Phys. Lett. A 374 (2010) 3038-3041. DOI: [10.1016/j.physleta.2010.05.033](https://doi.org/10.1016/j.physleta.2010.05.033)
- [38] G. Martin, C. Sabathier, J. Wiktor, S. Maillard, « *Molecular dynamics study of the bulk temperature effect on primary radiation damage in uranium dioxide* », Nucl. Inst. Meth. Phys. Res. B 352 (2015) 135-139. DOI: [10.1016/j.nimb.2014.12.008](https://doi.org/10.1016/j.nimb.2014.12.008)
- [39] JH. Evans, « *Effect of temperature on bubble precipitation in uranium dioxide implanted with krypton and xenon ions* », J. Nucl. Mater. 188 (1992) 222-225. DOI: [10.1016/0022-3115\(92\)90475-Z](https://doi.org/10.1016/0022-3115(92)90475-Z)
- [40] A. Michel, C. Sabatier, G. Carlot, O. Kaitasov, S. Bouffard, P. Garcia, C. Valot, « *An in situ TEM study of the evolution of Xe bubble populations in UO₂* », Nucl. Inst. Meth. Phys. Res. B 272 (2011) 218-221. DOI: [10.1016/j.nimb.2011.01.069](https://doi.org/10.1016/j.nimb.2011.01.069)
- [41] P. Martin, P. Garcia, G. Carlot, C. Sabathier, C. Valot, V. Nassif, O. Proux, J.-L. Hazemann, « *XAS characterisation of xenon bubbles in uranium dioxide* », Nucl. Inst. Meth. Phys. Res. B. 266 (2008) 2887-2891. DOI: [10.1016/j.nimb.2008.03.180](https://doi.org/10.1016/j.nimb.2008.03.180)
- [42] P.M. Martin, E. Vathonne, G. Carlot, R. Delorme, C. Sabathier, M. Freyss, P. Garcia, M. Bertolus, P. Glatzel, O. Proux, « *Behavior of fission gases in nuclear fuel: XAS characterization of Kr in UO₂* », J. Nucl. Mater, 466 (2015) 379-392. DOI: [10.1016/j.jnucmat.2015.08.019](https://doi.org/10.1016/j.jnucmat.2015.08.019)
- [43] Y. Yun, H. Kim, H. Kim, K. Park, « *Atomic diffusion mechanism of Xe in UO₂* », J. Nucl. Mater. 378 (2008) 40-44. DOI: [10.1016/j.jnucmat.2008.04.013](https://doi.org/10.1016/j.jnucmat.2008.04.013)
- [44] D.A. Andersson, B.P. Uberuaga, P.V. Nerikar, C. Unal, and C.R. Stanek, « *U and Xe transport in UO_{2+x}: Density functional theory calculations* », Phys. Rev. B 84 (2011) 054105. DOI: [10.1103/PhysRevB.84.054105](https://doi.org/10.1103/PhysRevB.84.054105)
- [45] S.T. Murphy, A. Chartier, L. Van Brutzel, J.-P. Crocombette, « *Free energy of Xe incorporation at point defects and in nanovoids and bubbles in UO₂* », Phys. Rev. B 85 (2012) 144102. DOI: [10.1103/PhysRevB.85.144102](https://doi.org/10.1103/PhysRevB.85.144102)
- [46] E. Moore, L.R. Corrales, T. Desai, R. Devanathan, « *Molecular dynamics simulation of Xe bubble nucleation in nanocrystalline UO₂ nuclear fuel* », J. Nucl. Mater. 419 (2011) 140-144. DOI: [10.1016/j.jnucmat.2011.08.052](https://doi.org/10.1016/j.jnucmat.2011.08.052)
- [47] F. Gupta, A. Pasturel, G. Brillant, « *Ab initio study of solution energy and diffusion of caesium in uranium dioxide* », J. Nucl. Mater. 385 (2009) 368-371. DOI: [10.1016/j.jnucmat.2008.12.009](https://doi.org/10.1016/j.jnucmat.2008.12.009)
- [48] V.F. Chkvaseli, H.J. Matzke, « *Fission-gas bubble behavior in uranium dioxide* », J. Nucl. Mater. 201 (1993) 92-96. DOI: [10.1016/0022-3115\(93\)90162-R](https://doi.org/10.1016/0022-3115(93)90162-R)
- [49] JH. Evans, « *Bubble diffusion to grain boundaries in UO₂ and metals during annealing – a new approach* », J. Nucl. Mater. 210 (1994) 21-29. DOI: [10.1016/0022-3115\(94\)90218-6](https://doi.org/10.1016/0022-3115(94)90218-6)
- [50] M.S. Veshchunov, V.E. Shestak, « *An advanced model for intragranular bubble diffusivity in irradiated UO₂ fuel* », J. Nucl. Mater. 376 (2008) 174-180. DOI: [10.1016/j.jnucmat.2008.01.026](https://doi.org/10.1016/j.jnucmat.2008.01.026)
- [51] L. Verma, L. Noirot, P. Maugis, « *Modelling intragranular bubble movement and fission gas release during post-irradiation annealing of UO₂ using a meso scale and spatialized approach* », J. Nucl. Mater. 528 (2020) 151874. DOI: [10.1016/j.jnucmat.2019.151874](https://doi.org/10.1016/j.jnucmat.2019.151874)
- [52] R.W. Grimes, C.R.A. Catlow, « *The stability of fission products in uranium dioxide* », Phil. Roy. Trans. Soc. London. A 335 (1991) 609. DOI: [10.1098/rsta.1991.0062](https://doi.org/10.1098/rsta.1991.0062)
- [53] C.T. Walker, C. Bagger, M. Mogensen, « *Observations on the release of cesium from UO₂ fuel* », J. Nucl. Mater. 240 (1996) 32-42. DOI: [10.1016/S0022-3115\(96\)00477-1](https://doi.org/10.1016/S0022-3115(96)00477-1)
- [54] T. Wiss, O. Dieste-Blanco, A. Tacu, Z. Talip, J.-Y. Colle, P. Martin, R.J.M. Konings, « *TEM study of alpha-damaged plutonium and americium dioxides* », J. Mater. Res. 30 (2015) 1544-1554. DOI: [10.1557/jmr.2015.37](https://doi.org/10.1557/jmr.2015.37)
- [55] A.S. Boyarchenkov, S.I. Potashnikov, K.A. Nekrasov, A.Y. Kupryazhkin, « *Investigation of cation self-diffusion mechanisms in UO_{2+x} using molecular dynamics* », J. Nucl. Mater. 442 (2013) 148-161. DOI: [10.1016/j.jnucmat.2013.08.030](https://doi.org/10.1016/j.jnucmat.2013.08.030)

- [56] J. Rest, MWD Cooper, J. Spino, JA Turnbull, P. Van Uffelen, CT Walker, « *Fission gas release from UO₂ nuclear fuel: A review* », J. Nucl. Mater. 513 (2019) 310-345. DOI: [10.1016/j.jnucmat.2018.08.019](https://doi.org/10.1016/j.jnucmat.2018.08.019)
- [57] L. He, XM. Bai, J. Pakarinen, BJ Jaques, J. Gan, AT. Nelson, A. El-Azab, TR. Allen, « *Bubble evolution in Kr-irradiated UO₂ during annealing* », J. Nucl. Mater. 496 (2017) 242-250. DOI: [10.1016/j.jnucmat.2017.09.036](https://doi.org/10.1016/j.jnucmat.2017.09.036)